Evaluation of Novel Whole-Body High-Resolution Rodent SPECT (Linoview) Based on Direct Acquisition of Linogram Projections

Stephan Walrand, PhD[1]; François Jamar, MD, PhD[1]; Marion de Jong, PhD[2]; and Stanislas Pauwels, MD, PhD[1]

[1]Laboratory of Molecular Imaging and Experimental Radiotherapy, Université Catholique de Louvain, Brussels, Belgium; and
[2]Department of Nuclear Medicine, Erasmus MC, Rotterdam, The Netherlands

Studies of the biodistribution of radiolabeled compounds in rodents frequently are performed during the process of development of new pharmaceutical drugs. This article presents the evaluation of a new whole-body animal SPECT system, called the Linoview SPECT system. **Methods:** Linoview SPECT is based on the linear orbit acquisition technique associated with slit-aperture collimators mounted on 4 pixelated CsI(Na) detectors composed of an array of small, individual crystal elements. Sliding iridium rods allow variation of the collimator aperture. Hot-rod and cold-rod phantoms filled with ^{99m}Tc were imaged. Mice were imaged, and kidney radioactivity was measured after injection of ^{99m}Tc-dimercaptosuccinic acid and ^{111}In-diethylenetriaminepentaacetic acid-D-Phe[1]-octreotide (^{111}In-pentetreotide; OctreoScan^{111}). **Results:** Phantom studies showed that hot rods separated by 0.35 mm can be distinguished and that 0.65-mm-diameter cold rods can be visualized, both at low-counting-rate acquisitions (111 and 59 MBq $\times$ h, respectively). In both mouse studies, the SPECT images allowed a clear delineation of the radioactivity concentrated over the cortex area of the kidneys, whereas the pelvis and the pelviureteral junction (1 mm) appeared as cold areas. The quantitative data derived from SPECT were in good agreement with the radioactivity counting obtained with a γ-counter after isolation of the kidneys. In addition, in the mouse injected with ^{111}In-pentetreotide, the kidney radioactivity distribution seen with SPECT was in agreement with the ex vivo autoradiograms of the isolated kidneys. **Conclusion:** The phantom studies showed a clear improvement of the spatial resolution over the results reported in the literature with other dedicated small-animal SPECT systems, especially in cold-rod phantom studies. The increased performance can be ascribed to the high stability of the system with regard to the statistical noise present in the acquired data. The mouse studies showed that this system will be most useful for in vivo high-resolution SPECT and quantitative biodistribution studies in rodents, even with medium-energy radioisotopes that are difficult to image, such as ^{111}In.

Key Words: small-animal imaging; animal SPECT; SPECT; linogram; high-resolution imaging

J Nucl Med 2005; 46:1872–1880

The early phase of development of new drugs frequently requires pharmacokinetic and biodistribution studies in rodents. The biodistribution of a compound commonly is assessed by ex vivo autoradiography with a radiolabeled analog of the native compound. Such studies involve the sacrifice of series of animals at several time points after injection of the compound. Until now, in vivo imaging techniques were not able to substitute for this ex vivo approach because of a lack of spatial resolution. However, an in vivo method such as SPECT could provide several benefits. First, studies of the biodistribution of a radiolabeled molecule or comparison between different ones could be achieved in the same animal, thereby avoiding interindividual variance. Second, fast dynamic studies starting at the time of drug injection should be achievable and provide pharmacokinetic information. Third, the possibility of monitoring the animal over a long period of time could simplify the assessment of drug therapy. Finally, this approach also could circumvent the complexity of ex vivo autoradiography and reduce the number of animals used, resulting in lower costs of drug development, especially if genetically engineered animals are needed. Furthermore, a reduction in the number of animals that are sacrificed is a very valuable feature from an ethical point of view.

Over the last few years, many efforts have been directed toward improving the performance of small-animal SPECT. Improvement in the spatial resolution was addressed by the use of pixelated detectors (i.e., composed of an array of small individual crystal elements) rather than a continuous scintillator and by the use of pinhole collimators rather than parallel- or convergent-hole collimators (*1–3*). However, SPECT remains an ill-posed problem, highly sensitive to the

noise present in the acquired data (*4*). A way to reduce this noise is to increase the efficiency of the detection with either 3-dimensional (3D) SPECT or multipinhole collimators (*5–9*). In 3D SPECT, collimation in 1 direction is removed, a process that dramatically improves sensitivity. However, a significant portion of the information about the incoming direction of the γ-rays is lost. To compensate for this missing information, 3D methods use additional detector motion, usually rotation of the collimator around its radial axis. With pinhole collimation, the set of tomographic data is complete only in the transverse plane passing through the pinhole aperture. Complex acquisition orbits therefore are needed to avoid axial blurring (*10–12*). Alternatively, sophisticated iterative reconstruction algorithms, taking into account the fact that data are missing, may improve the pinhole longitudinal field of view.

We attempted to improve system performance by enhancing sensitivity and acquiring information about the direction of the γ-rays as accurately as possible. The system evaluated is based on the linear orbit acquisition (LOrA) technique already proposed for human application (*13*). In LOrA SPECT, the revolution orbit around the target is replaced by a rectangular orbit. As already noted by Edholm et al. (*14*), in the case of a transmission system, this association of fanbeam geometry with relative translation of the target provides direct linogram acquisition rather than the classical sinogram. The LOrA technique requires only the use of a convergent collimator with a full opening angle of 90° in the transverse plane, for example, a pinhole or a multipinhole collimator. The immediate benefit is that LOrA allows setting of the collimator aperture closer to the animal boundary without any loss of data completeness or truncation problems. This feature increases both the efficiency and the spatial resolution without deterioration of the noise stability of the tomographic reconstruction. For the purpose of a whole-body biodistribution study, the use of a hybrid fanbeam collimator, combining a slit aperture and septal collimation forming a rake (*15,16*), was evaluated to avoid the overlap of γ-rays on the detector. The disadvantage of fanbeam geometry is that it has lower sensitivity and spatial resolution in the axial direction than does pinhole geometry. However, with the Linoview SPECT device, the sensitivity loss is compensated for by positioning of the collimator closer to the target, and the axial spatial resolution loss is compensated for by translation in the axial direction. The fanbeam geometry allows the use of simple orbital motion while preserving the tomographic completeness of the acquired data for the whole body length.

The aim of this study was to evaluate the performance of Linoview SPECT with hot-rod and cold-rod phantoms as well as with mouse models. Hot-rod phantoms were used to evaluate the benefit of the use of iridium as aperture material. Cold-rod phantoms were used to estimate the noise stability of the system.
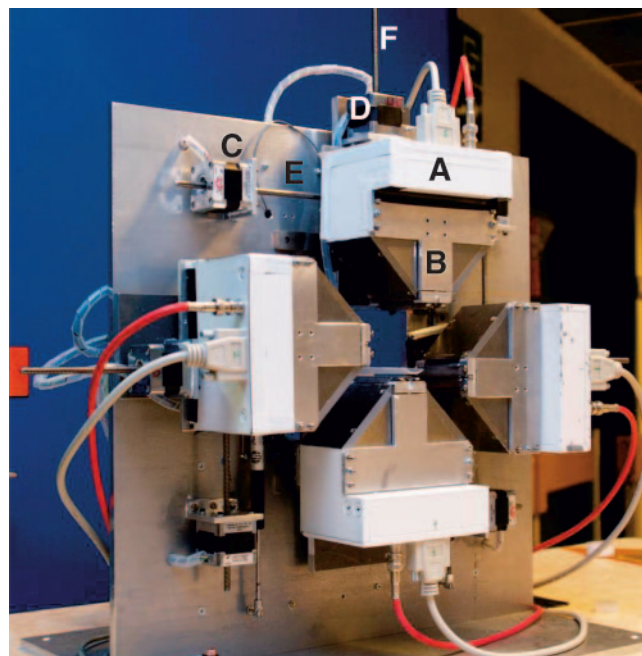

FIGURE 1. Linoview SPECT device (Linoview Systems), consisting of 4 pixelated CsI(Na) detectors (A) associated with rake collimator (B). Orbital and radial motions are obtained with stepper motors (C and D) acting on endless screws (E and F).

MATERIALS AND METHODS

Linoview SPECT Device

The animal Linoview SPECT device (Linoview Systems; Fig. 1) is based on four 2- by 5-in. γ-ray detectors (Rayvision). Ten 1- by 1-in. position-sensitive photomultiplier tubes per detector (R8520-00-C12; Hamamatsu Photonics) are coupled to a pixelated CsI(Na) scintillator (5-mm thickness, 21×52 pixels of 2.5×2.5 mm). The detectors are connected to a computer via an analog-to-digital board (PCI-416; Datel) driven by the acquisition software KmaxNT (Sparrow Corp.). The intrinsic spatial resolution is 2.5 mm, the intrinsic energy resolution at 140 keV is 35%, and the intrinsic sensitivity in an energy window of 35% width centered on the photopeak is 42%. The collimator and detector housings are made of tungsten alloy (W-Ni-Fe; W, 95%; density = 18; thickness, 7 mm [XiAn Tungsten & Alloy]). The rake collimator has a slit aperture parallel to the longitudinal direction (Fig. 2A). This tunable slit aperture is composed of 2 square iridium rods ($2 \times 2 \times 60$ mm) inserted in 2 linear sliding holders made of tungsten alloy (Fig. 2B), allowing a slit width of 0–5 mm. The distance between the slit aperture and the scintillator surface is 62 mm. Longitudinal collimation is achieved by 20 parallel trapezoidal tungsten sheets (55 mm high, 125-mm bottom width, 16-mm top width, 0.5-mm thickness, 2-mm interspace) sandwiched in a nonattenuating medium (extruded polystyrene) (Fig. 2C). The radial and orbital motions are managed by linear slide guides (MNN18-G3; Sheenberger) and stepper motors acting on an endless screw (L1MGB; EAD Motors), driven by a controller board (DCB-261; AMS). Mechanical limit switches serve as reference points. All linear guides and stepper motors are mounted on an aluminum plate with a position accuracy of 0.1 mm.

The physical dimensions needed for the tomographic reconstruction are the focal length of the collimators, the distance from
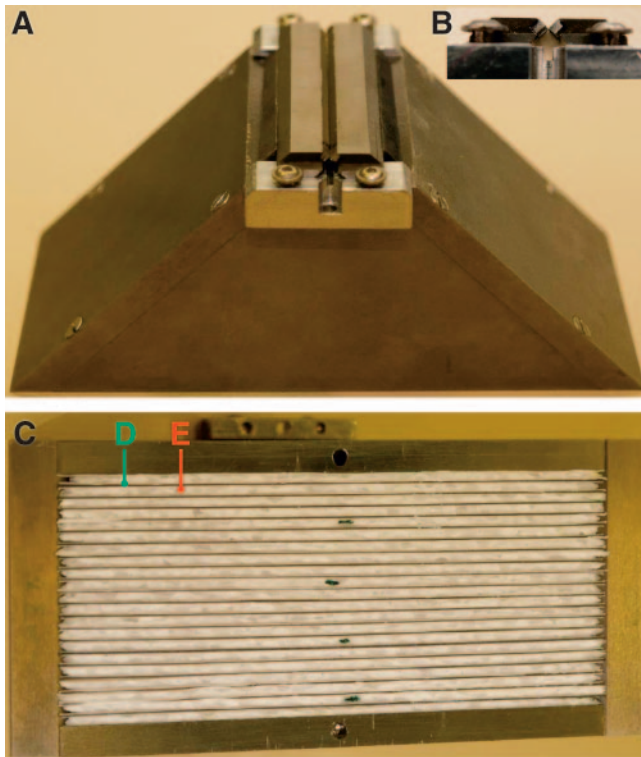
FIGURE 2. Collimators. (A) Upper view of collimator with adjustable slit aperture parallel to longitudinal direction. (B) Lateral view of 2 square iridium rods inserted in tungsten holders. (C) Inferior view of collimator showing tungsten sheets (D) sandwiched in extruded polystyrene (E).

the slit aperture to the axis origin, the transverse position of the slit aperture on the crystal, and the slit aperture position along the orbit. All of these parameters were obtained by a calibration procedure consisting of 3 tomographic acquisitions of a linear source located approximately at the transverse coordinates (-5, -5 mm), ($+5$, -5 mm), and (-5, $+5$ mm). A numeric program automatically computes the actual source positions and physical dimensions of the system (Appendix). The benefit of this procedure is to avoid difficult direct measurements of distances. Furthermore, it is automatic and provides the effective dimensions of the system, taking into account γ-ray penetration into the edges of the iridium rods and into the crystal. As a result, the computed effective focal length is somewhat greater than that obtained by direct measurements.

Acquisition

The orbit ranges of the detectors were set in such a way that the 4 slit apertures would draw the narrowest rectangle possible around the object to be imaged. The distance between the slit aperture and the phantom or the animal boundary was typically about 3 mm. Acquisitions were performed in continuous motion. The acquired data were stored in list mode and including the following: detector number, (x, y) event position, event time (ms), and event energy (256 channels).

Reconstruction

Events from the list mode file with an energy within a 50% window centered on the photopeaks were rebinned in matrix (d,r,z,v), in which $d \in [0,3]$ was the detector number, $r \in [0,51]$ was the transverse coordinate of the scintillator pixel hit, $z \in [0,20]$ was its longitudinal coordinate, and $v \in [0,511]$ was the coordinate along the linear orbit corresponding to an orbit step size of about 0.05 mm, depending on the size of the object to image. All linograms were reconstructed by use of the expectation maximization maximum likelihood (EM-ML) algorithm without attenuation, scatter correction, or spatial resolution recovery (17,18). No noise filtering was applied. The number of iterations and pixel size were chosen visually to obtain a good noise-to-spatial resolution compromise and are shown in Tables 1 and 2. It should be noted that linograms allow the use of fast projection and backprojection algorithms, such as approximate discrete Radon transform (ADRT), resulting in an EM-ML reconstruction speed similar to that of ordered-subset expectation maximization (OSEM) (19). However, in this first evaluation of the system, the projection and backprojection steps in the EM-ML algorithm were performed simply by numeric integration along the lines passing through the slit aperture.

Phantoms

Two sets of hot-rod phantoms filled with ^{99m}Tc were used to estimate the spatial resolution: 1 set had an outer diameter of 30.5 mm, comparable to a mouse whole-body acquisition, and another set had an outer diameter of 22.5 mm, comparable to a brain acquisition (Table 1). The maximal activity $\times$ acquisition time used was 111 MBqh. A last set of cold-rod phantoms was used to test the sensitivity of the system against noise (Table 2). The outer diameter of the cold-rod phantoms was 31.5 mm, comparable to a mouse whole-body acquisition, and the maximal activity $\times$ acquisition time used was 59 MBqh.

The activity $\times$ acquisition times shown in Tables 1 and 2 correspond to the activity in the reconstructed slices described in

TABLE 1
Hot-Rod Phantom Characteristics

Phantom	Phantom diameter* (mm)	Rod diameter (mm)	Distance between rod edges (mm)	Activity $\times$ acquisition time (MBqh)	Collimator aperture (mm)	EM-ML iterations (n)	Reconstruction matrix pixel size (mm)
1	30.5	0.75	0.75	32	0.20	128	0.35
2	30.5	0.45	0.35	57	0.10	1,100	0.18
3	22.5	0.50	0.50	34	0.20	128	0.25
4	22.5	0.45	0.35	111	0.10	900	0.18

*Phantom diameters of 30.5 and 22.5 mm were chosen to simulate mouse body and head, respectively.

TABLE 2
Cold-Rod Phantom Characteristics

Phantom	Phantom diameter* (mm)	Rod diameter (mm)	Distance between rod edges (mm)	Activity × acquisition time (MBqh)	Collimator aperture (mm)	EM-ML iterations (n)	Reconstruction matrix pixel size (mm)
1	31.5	2.50	2.00	18	0.20	16	1.20
2	31.5	1.30	1.50	24	0.20	32	0.60
3	31.5	0.65	0.75	59	0.20	160	0.25

*Phantom diameter of 31.5 mm was chosen to simulate mouse body.

Results. All of the acquisitions can be considered low-counting-rate acquisitions compared with what is generally used in such phantom studies (2,3,5). Acquisitions were performed with a slit width of 0.2 mm.

99mTc-Dimercaptosuccinic Acid (99mTc-DMSA) and 111In-Diethylenetriaminepentaacetic Acid-D-Phe1-Octreotide (111In-Pentetreotide) Imaging in Mice

Animal experiments were performed in compliance with the regulations of our institutions and with generally accepted guidelines governing such work. Two mice were imaged after injection of tracers known to be retained by the renal cortex; 1 tracer was labeled with 99mTc, and the other was labeled with 111In.

A 20-g wild-type male mouse was injected with 22 MBq of 99mTc-DMSA (TechneScan DMSA; Tyco HealthCare) and scanned 5 h after injection. A 22-g wild-type female mouse was injected with 11 MBq of 111In-pentetreotide (OctreoScan111; Tyco HealthCare) and scanned 24 h after injection.

Mice were anesthetized with ketamine (100 μg/g; Merial) and xylazine (10 μg/g; Bayer). Imaging was performed with a slit width of 0.4 mm. Five acquisitions of 5 min each were performed, the bed being shifted by 0.5 mm between acquisitions, resulting in reconstructed transverse slices 2 mm thick. The reconstructed pixel size was 0.5 mm, and 64 iterations were performed. The purpose of the multibed acquisition was to obtain the same pixel pitch (0.5 mm) in the longitudinal and transverse directions of the reconstructed volume. This process improves the visual quality of the coronal or sagittal slice. Regions of interest surrounding the kidneys were drawn plane by plane on all of the transverse SPECT slices. The activity in a region of interest was corrected by an attenuation factor equivalent to 1 cm of soft tissue and was expressed as a percentage of the injected activity. These quantitative data derived from SPECT were compared with the ex vivo measurements of radioactivity obtained with a γ-counter after isolation of the kidneys.

In the mouse injected with 111In-pentetreotide, 1 kidney was frozen quickly after isolation and further processed for cryosectioning and autoradiography. Tissue sections (10 μm) were mounted on glass slides. Sections were exposed to phosphorimaging screens (Packard Instrument Co.) in x-ray cassettes. The screens were analyzed by use of a Cyclone phosphorimager (Packard Instrument Co.).

RESULTS

Whole-Body Phantom

With a 0.20-mm collimator aperture, all of the 0.75-mm hot rods were clearly distinguishable on the whole slice (2 mm thick), whereas with a 0.1-mm aperture, the hot rods separated by 0.35 mm were distinguishable up to a 10-mm depth (Fig. 3). The active ring surrounding the 0.75-mm hot-rod phantom was the activity located between the acrylic disk and the inner wall of the phantom housing.

Brain Phantom

The 0.50-mm hot rods were clearly distinguishable on the whole slice (2 mm thick), whereas the hot rods separated by 0.35 mm were clearly distinguishable up to a 10-mm depth in the phantom and remained distinguishable in the central region, although the image was somewhat blurred (Fig. 4). Some activity was present between the phantom housing and the acrylic disks that were obtained by manual cutting.

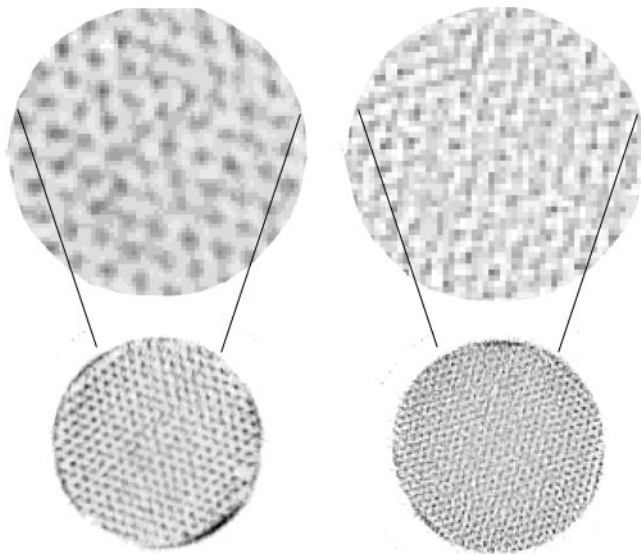#### 31.5-mm-Diameter Cold-Rod Phantom

With a 0.2-mm collimator aperture, both the 2.5-mm and the 1.3-mm cold rods were clearly visible on the whole slice (10 mm thick) of the phantom, whereas the 0.65-mm rods were clearly visible up to a 12-mm depth in the phantom and remained visible in the central region, with some blurring (Fig. 5).

99mTc-DMSA and 111In-Pentetreotide Imaging in Mice

Figure 6 shows coronal and transverse slices through mouse kidneys obtained 5 h after injection of 99mTc-DMSA and 24 h after injection of 111In-pentetreotide. Both tracers were concentrated over the cortex area, whereas no activity
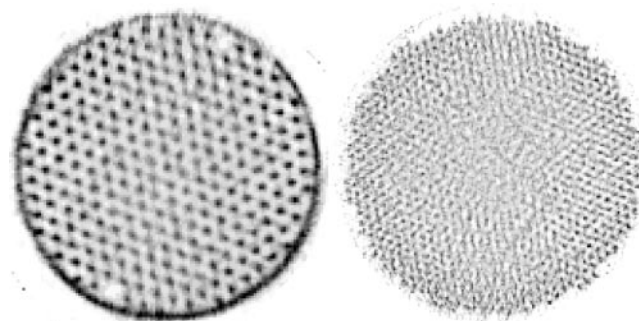
FIGURE 3. Transverse slices of two 30.5-mm-diameter hot-rod phantoms filled with 99mTc; acquisition statistics were 32 MBqh (left) and 57 MBqh (right). Distances between rod edges were 0.75 mm (left) and 0.35 mm (right). This distance determines spatial resolution achieved.

FIGURE 4. Transverse slices of two 22.5-mm-diameter hot-rod phantoms filled with [99mTc]; acquisition statistics were 34 MBqh (left) and 111 MBqh (right). Distances between rod edges were 0.50 mm (left) and 0.35 mm (right). This distance determines spatial resolution achieved. Top slices represent enlargement (factor 3) of central region of phantoms.

was seen in the pelvis or pelviureteral junction (~1-mm diameter). The kidney uptake values calculated from in vivo SPECT ([99mTc], 15.6 percentage injected dose [%ID]; [111In], 9.1 %ID) were similar to those obtained ex vivo by γ-counting ([99mTc], 15.2 %ID; [111In], 9.6 %ID).

DISCUSSION

The results obtained with this animal SPECT system indicate a significant improvement in spatial resolution over those obtained with other dedicated small-animal SPECT systems. The improvement is spectacular, especially with cold-rod phantoms. Indeed, high-contrast images were obtained with 1.3-mm cold rods and low acquisition statistics (24 MBqh), whereas in the literature, images obtained with cold rods of the same size usually have had much less contrast, even with high acquisition statistics, such as 333, 1,850, and 2,146 MBqh (2–3,5). With 0.65-mm cold rods and 59 MBqh, all of the rods still were visualized, but with lower contrast, which was particularly marked in the center of the phantom. Different factors, such as the collimator design and direct linogram acquisition, contribute to this improvement.
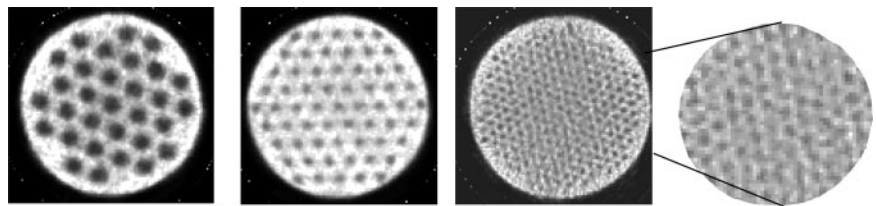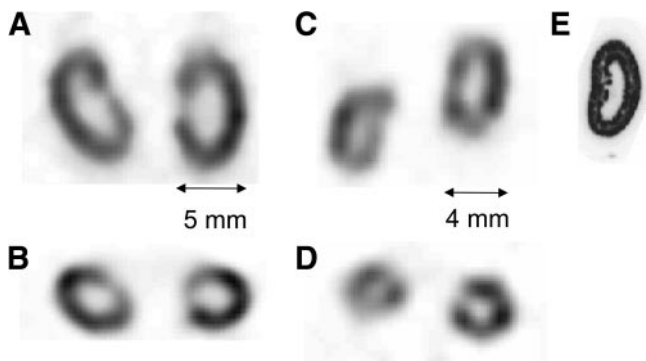
In rod phantoms in which the radioactivity is spread over an extended area, the spatial resolution depends significantly on the long-range tail of the collimator point spread function (PSF). Iridium was used as the material for the slit aperture instead of a tungsten alloy. Besides uranium, iridium is the most effective material for γ-ray attenuation. Its attenuation coefficient is 39 cm^{-1} at 150 keV; that for tungsten is 30 cm^{-1} (20). The increased stopping power results in a faster decrease in the collimator PSF tail. Also, the use of a tunable slit allows very small apertures; when the 2 iridium parts are set in contact with each other at 140 keV, the effective aperture is 0.22 mm as a result of the γ-ray penetration. Furthermore, it was already shown that for a similar collimator spatial resolution, the translation of this spatial resolution in the reconstructed transverse plane with LOrA leads to a spatial resolution better than that obtained with a classical revolution orbit in the center of the reconstructed slice (13).

In the cold-rod phantoms, the active region represents almost the whole phantom volume. The challenge is to distinguish the small cold regions from the reconstruction artifacts generated by the surrounding activity. Thus, the image quality depends strongly on the signal-to-noise ratio. This ratio can be improved by 2 ways: by reducing the noise present in the acquired data and by increasing the noise stability of the tomographic system.

With the classical revolution orbit, or stationary multipinhole system, the positioning of the animal close to the collimator aperture introduces truncation problems in the reconstruction process. The latter problems generally are solved by increasing the radius (≥25 mm); unfortunately, this process leads to a reduction in spatial resolution and sensitivity. In contrast, LOrA allows setting the collimator closer to the animal without missing any data (13). As a result, the optimal efficiency and spatial resolution of the collimator are used without introducing truncation problems and without altering the stability of the reconstruction process. For example, in a mouse brain study, the brain center can be positioned ~10 mm away from the collimator aperture. In such a setting, a LOrA SPECT system equipped with a 0.89-mm-diameter pinhole collimator would provide a spatial resolution similar to that obtained with a classical SPECT system equipped with a 0.3-mm-diameter pinhole collimator (Fig. 7A). These latter 2 factors—reduced distance from collimator to target and larger collimator aperture—would lead to a theoretic improvement in sensitivity by a factor of ~60 in favor of a LOrA SPECT system

FIGURE 5. Transverse slices of three 31.5-mm-diameter cold-rod phantoms filled with [99mTc]; acquisition statistics were 18, 24, and 59 MBqh (from left to right). Diameters of cold rods were 2.50, 1.30, and 0.65 mm (from left to right). Slice at right represents enlargement (factor 2) of central region of 0.65-mm-diameter cold-rod phantom.

FIGURE 6. Coronal (A and C) and transverse (B and D) slices through kidneys of 20-g male mouse imaged 5 h after injection of 22 MBq of ^{99m}Tc-DMSA (A and B) and 22-g female mouse imaged 24 h after injection of 11 MBq of ^{111}In-pentetreotide (C and D). For both acquisitions, distance between mouse center and collimator aperture was 16 mm. Note that tracer was concentrated over cortex area, whereas no activity was seen in pelvis or pelviureteral junction ($\approx$1-mm diameter). (E) Similar pattern of activity distribution was seen on ex vivo autoradiogram obtained for mouse injected with ^{111}In-pentetreotide.

compared with a classical SPECT system (Fig. 7B). In this configuration, a LOrA SPECT system with 4 detectors equipped with pinhole collimators would be equivalent to a 240-multipinhole system.

Another major feature of the implementation of LOrA is that it directly provides linograms rather than the usual sinograms. Although a point source acquired with a converging collimator along a revolution orbit does not exactly result in a sinusoidal curve but presents some distortion, the following considerations are still valid (*21*). Considering the limit of infinitely fine sampling, both linogram and sinogram acquisitions provide a complete set of data allowing an exact tomographic reconstruction. In a real study, one must deal with discrete data sampling and reconstruction of a discrete matrix. Tomography is known to be an ill-posed problem resulting in an amplification of the noise present in the acquired data during the reconstruction process (*4*). However, linograms are known to provide data sampling different from that provided by sinograms. This feature is clearly visible in the Fourier space of frequencies, in which linograms provide samples of the Fourier transform on radial points located on concentric equidistant squares (pseudopolar Fourier transform) rather than on radial points located on equidistant circles, as with sinograms (*21*). Besides the fact that this difference allows faster computation in direct Fourier reconstruction (*14*), work in progress suggests that, in contrast to sinograms, linograms offer a discrete Radon transform that is algebraically exact and invertible (*22*). Furthermore, in sinogram reconstruction, the transverse coordinate on the detector plays the role of a radial coordinate, and oversampling of the sinogram on this coordinate allows reduction of the noise present in the reconstructed slice (*23*). However, this radial oversampling is hampered by the finite spatial resolution of the detector.

In contrast, in linogram reconstruction, because the transverse coordinate on the detector is replaced by the coordinate of the detector on the orbit, there is no restriction of the subsequent radial oversampling (*13*). Further work should be conducted to evaluate whether these properties could improve the stability of the system against the noise present in the acquired data. Such improvement in stability could be an additional explanation for the good results obtained for cold-rod phantoms.

Preliminary studies with mice confirmed the initial phantom results in that a high spatial resolution could be reached with low activities (11–22 MBq); the SPECT images allowed a clear delineation of the radioactivity concentrated over the cortex area of the kidneys, whereas the pelvis and the pelviureteral junction (1 mm) appeared as cold areas. Furthermore, the quantitative data derived from SPECT
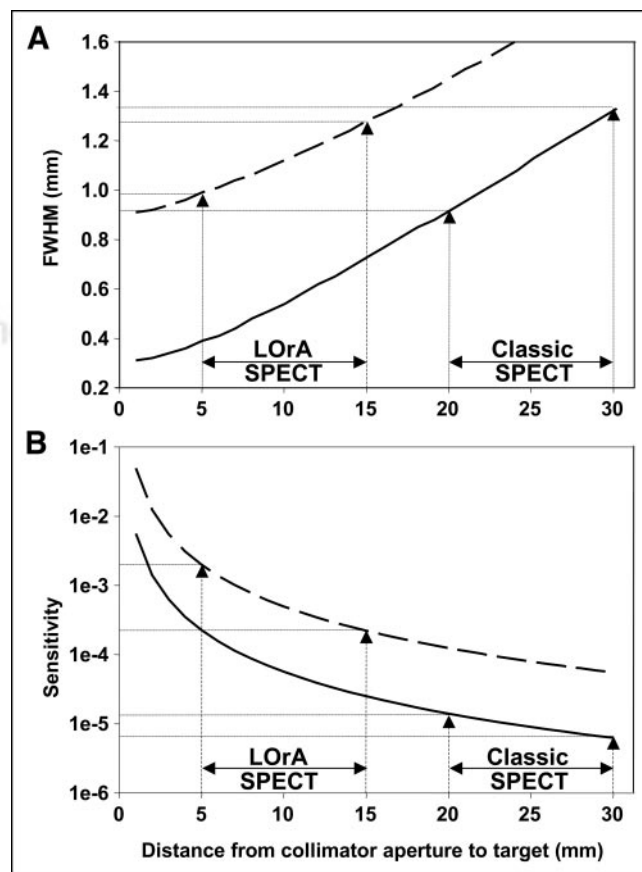
FIGURE 7. Theoretic spatial resolution (A) and sensitivity (B) for pinhole collimator (60-mm collimator focal length, 2.5-mm detector intrinsic spatial resolution) as function of target-to-aperture distance. When imaging small target organ, for example, mouse brain, organ would be positioned much closer to collimator aperture in LOrA SPECT (5–15 mm) than in classical SPECT (20–30 mm). As a result, LOrA SPECT equipped with 0.89-mm-effective-diameter pinhole (dashed line) provides spatial resolution similar to that obtained with classical SPECT and 0.30-mm-effective-diameter pinhole (solid line). These 2 factors, increased hole diameter and reduced target-to-aperture distance, lead to improvement in sensitivity by factor of ~60 in center of organ. FWHM = full width at half maximum.

were similar to those obtained by ex vivo counting in the isolated organs. In addition, in the mouse injected with ^{111}In-pentetreotide, the kidney radioactivity distribution seen with SPECT was in agreement with the ex vivo autoradiogram (Fig. 6E).

The use of a rake collimator, which has a fanbeam geometry, ensures the completeness of the acquired data along the whole body length without the need for a sophisticated orbit (10–12); the whole body can be imaged in 1 linear motion of the detectors. This simple linear motion can be achieved in a very short time (~5 s) compatible with dynamic SPECT after tracer injection. For this purpose, the tunable slit can be opened up to 5 mm to increase sensitivity, when needed. The scan range in the longitudinal direction was 5 cm in this prototype but could be increased; 7.5 cm should be appropriate for whole-body studies with mice, and 15 cm should be appropriate with rats. The current rake collimator was designed for whole-body pharmacokinetic studies and provided a 2-mm thickness for reconstructed slices. Multibed acquisitions—with a bed shift of 0.5 mm between acquisitions—provided high-quality coronal images of small organs, such as the kidneys. In the future, longitudinal spatial resolution recovery for multibed acquisitions should be implemented in the reconstruction program and evaluated. Further, the use of a slanted rake collimator also focusing in the longitudinal direction or a pinhole collimator should be evaluated for dedicated organ studies.

The major drawback of the current prototype is the flatness of the γ-detector used. As a consequence, the distance from the aperture to the detector edge is $\sqrt{2}$ longer than the distance to the detector center, reducing the local sensitivity by a factor of ~2. Also, at the edge of the detector, the γ-rays reach the crystals at an incident angle of 45°, leading to an alteration in the spatial resolution. Indeed, because of γ-ray penetration into the crystals, a signal will be generated not only in the crystal directly hit by the γ-rays but also in adjacent crystals. The resulting spatial resolution deterioration already noted with ^{99m}Tc is much more pronounced with high-energy radionuclides, such as ^{111}In. In the future, a cylindric design of the γ-detector would overcome the 2 problems described here. In such a design, the increase in crystal thickness would further improve the system sensitivity without altering the spatial resolution.

Because of the low-energy resolution of the system, the scattered γ-rays cannot be rejected and will alter to some extent the image resolution. Using a system equipped with a rake collimator and a detector with similar pixel size and energy resolution, Brasse et al. showed that ~20% of the detected photons were scattered inside the mouse and 1% were scattered inside the collimator (16). Therefore, in the future, the system also should benefit from the use of cadmium-zinc-telluride (CZT) detectors, which offer better energy resolution.

CONCLUSION

Our studies showed that this new animal SPECT, based on linogram acquisitions, provides high-spatial-resolution images of cold and hot structures in the submillimeter range. The preliminary mouse studies showed that this system will be most useful for in vivo high-resolution SPECT and quantitative biodistribution studies with rodents, even with medium-energy radioisotopes that are difficult to image, such as ^{111}In.

APPENDIX

The linear sources used for the calibration procedure consisted of a glass capillary with a 1-mm inner diameter filled with either ^{99m}Tc or ^{111}In. Acquisitions were performed with the collimator aperture ~20 mm distant from the center of the gantry.

In a linogram acquired for slice z of source s, the coordinate (V_α) of detector α along its linear orbit was defined as follows:

$$V_\alpha = A^s_{\alpha z} r_\alpha + B^s_{\alpha z}, \qquad \text{Eq. 1A}$$

where r_α is the transverse coordinate of the γ-rays on detector α and $s = 0,1,2$ for the linear source positioned approximately at the coordinates (−5 mm, −5 mm), (5 mm, −5 mm), and (−5 mm, 5 mm) against the center of the gantry and parallel to the collimator aperture. As shown in the system view depicted in Figure 1, the horizontal x-axis is pointing to the right, the vertical y-axis is pointing to the top, and the longitudinal z-axis is parallel to the collimator aperture. The orbit coordinate V_α increases when the detectors move in the clockwise direction. The r axis on detector α points in the direction of the clockwise motion. The detectors are numbered from 0 to 3 in a clockwise fashion starting from the right detector (Fig. 1). The parameters $A^s_{\alpha z}$ and $B^s_{\alpha z}$ are obtained simply by performing a linear least-squares fitting of the maximum pixel in each line r of the linograms of Equation 1A.

Considering that the γ-rays cross the collimator aperture, the $A^s_{\alpha z}$ and $B^s_{\alpha z}$ parameters are described by the following equations:

$$A^s_{0z} = \frac{U_{0z} - x^s_2}{F_{0z}}, \qquad \text{Eq. 2A}$$

$$A^s_{1z} = \frac{U_{1z} + y^s_z}{F_{1z}}, \qquad \text{Eq. 3A}$$

$$A^s_{2z} = \frac{U_{2z} + x^s_z}{F_{2z}}, \qquad \text{Eq. 4A}$$

$$A^s_{3z} = \frac{U_{3z} - y^s_z}{F_{3z}}, \qquad \text{Eq. 5A}$$

$$B^s_{0z} = A^s_{0z}\delta r_{0z} - \delta V_{0z} - y^s_z, \qquad \text{Eq. 6A}$$

$$B^s_{1z} = A^s_{1z}\delta r_{1z} - \delta V_{1z} - x^s_z, \qquad \text{Eq. 7A}$$

$$B_{2z}^s = A_{2z}^s \delta r_{2z} - \delta V_{2z} + y_z^s, \qquad \text{Eq. 8A}$$

and

$$B_{3z}^s = A_{3z}^s \delta r_{3z} - \delta V_{3z} + x_z^s, \qquad \text{Eq. 9A}$$

where the unknowns are $U_{\alpha z}$, the distance between the aperture of detector α and the system axis parallel to the detector orbit; $F_{\alpha z}$, the effective focal length of detector α; δr_α, the offset of the actual aperture position from the detector coordinate origin; $\delta V_{\alpha z}$, the offset of the actual aperture position from the orbit coordinate V_α; and the source coordinates x_z^1, y_z^1, x_z^2, and y_z^2. The values for coordinates x_z^0 and y_z^0 can be fixed arbitrarily, and the chosen values will determine the axis system used for the reconstructed space; in our system, the values used were $x_z^0 = -5$ mm and $y_z^0 = -5$ mm.

From Equation 2A, we obtain

$$x_z^2 - x_z^0 = \frac{A_{0z}^2 - A_{0z}^0}{A_{0z}^1 - A_{0z}^0}(x_z^1 - x_z^0) = b(x_z^1 - x_z^0),$$

$$\text{Eq. 10A}$$

and from Equation 3A, we obtain

$$y_z^1 - y_z^0 = \frac{A_{0z}^1 - A_{0z}^0}{A_{0z}^2 - A_{0z}^0}(y_z^2 - y_z^0) = a(y_z^2 - y_z^0).$$

$$\text{Eq. 11A}$$

Elimination of $\delta V_{\alpha z}$ by subtraction in Equations 6A to 9A provides the following equations:

$$B_{0z}^0 - B_{0z}^1 = (A_{0z}^0 - A_{0z}^1)\delta r_{0z} + (y_z^1 - y_z^0),$$

$$\text{Eq. 12A}$$

$$B_{0z}^0 - B_{0z}^2 = (A_{0z}^0 - A_{0z}^2)\delta r_{0z} + (y_z^2 - y_z^0),$$

$$\text{Eq. 13A}$$

$$B_{1z}^0 - B_{1z}^1 = (A_{1z}^0 - A_{1z}^1)\delta r_{1z} + (x_z^1 - x_z^0),$$

$$\text{Eq. 14A}$$

$$B_{1z}^0 - B_{1z}^2 = (A_{1z}^0 - A_{1z}^2)\delta r_{1z} + (x_z^2 - x_z^0),$$

$$\text{Eq. 15A}$$

$$B_{2z}^0 - B_{2z}^1 = (A_{2z}^0 - A_{2z}^1)\delta r_{2z} - (y_z^1 - y_z^0),$$

$$\text{Eq. 16A}$$

$$B_{2z}^0 - B_{2z}^2 = (A_{2z}^0 - A_{2z}^2)\delta r_{2z} - (y_z^2 - y_z^0),$$

$$\text{Eq. 17A}$$

$$B_{3z}^0 - B_{3z}^1 = (A_{3z}^0 - A_{3z}^1)\delta r_{3z} - (x_z^1 - x_z^0),$$

$$\text{Eq. 18A}$$

and

$$B_{3z}^0 - B_{3z}^2 = (A_{3z}^0 - A_{3z}^2)\delta r_{3z} - (x_z^2 - x_z^0). \qquad \text{Eq. 19A}$$

Removing the source coordinates between each consecutive even–odd couple in Equations 12A to 19A by use of Equations 10A and 11A provides the following δr_α offsets:

$$\delta r_\alpha = \frac{(B_{\alpha z}^0 - B_{\alpha z}^1) - a(B_{\alpha z}^0 - B_{\alpha z}^2)}{(A_{\alpha z}^0 - A_{\alpha z}^1) - a(A_{\alpha z}^0 - A_{\alpha z}^2)} \quad \text{for} \quad \alpha = 0 \text{ or } \alpha = 2$$

$$\text{Eq. 20A}$$

and

$$\delta r_\alpha = \frac{b(B_{\alpha z}^0 - B_{\alpha z}^1) - (B_{\alpha z}^0 - B_{\alpha z}^2)}{b(A_{\alpha z}^0 - A_{\alpha z}^1) - (A_{\alpha z}^0 - A_{\alpha z}^2)} \quad \text{for} \quad \alpha = 1 \text{ or } \alpha = 3.$$

$$\text{Eq. 21A}$$

Now, the domino-falling process is initiated. Replacing the δr_α offsets in Equations 12A to 19A with their values in Equations 20A and 21A directly provides the source coordinates x_z^1, y_z^1, x_z^2, and y_z^2; the same operation in Equations 6A to 9A directly provides the $\delta V_{\alpha z}$ offsets; subtracting Equations 2A to 5A between sources 1 and 0 removes the unknown U_α and provides the effective focal length $F_{\alpha z}$; and replacing $F_{\alpha z}$, x_z^s, and y_z^s with their values in Equations 2A to 5A provides the actual distance $U_{\alpha z}$ used for the acquisitions.

The deviations of the glass capillary used for the linear source, of the square iridium rods, and of the linear sliding guides from a straight line are much smaller than the spatial resolution of the system; the same is true regarding the deviation of the crystal array surface from a flat plane. As a consequence, the variations in the actual parameters $\delta r_{\alpha z}$, $\delta V_{\alpha z}$, $F_{\alpha z}$, and $U_{\alpha z}$ along the longitudinal coordinate z are only attributable to spatial misalignments, mainly of the linear source and the collimator aperture (the detectors are heavy—~20 kg—and some flexing of the holders cannot be avoided). As a result, the actual parameters $\delta r_{\alpha z}$, $\delta V_{\alpha z}$, $F_{\alpha z}$, and $U_{\alpha z}$ are linear functions of the coordinate z. Thus, a linear fit of the computed parameters is applied to remove the fluctuations induced by the noise present in the acquired data. On the basis of our experience, 3 acquisitions of 30 s each with 7 MBq per millimeter of linear source are sufficient to obtain a reliable calibration of the system.

REFERENCES

1. McElroy DP, MacDonald LR, Beekman FJ, et al. Performance evaluation of A-SPECT: a high resolution desktop pinhole SPECT system for imaging small animals. *IEEE Trans Nucl Sci*. 2002;49:2139–2147.
2. MacDonald LR, Patt BE, Iwanczyk JS, et al. Pinhole SPECT of mice using the LumaGEM gamma camera. *IEEE Trans Nucl Sci*. 2001;48:830–836.
3. Acton PD, Choi SR, Plossl K, Kung HF. Quantification of dopamine transporters in the mouse brain using ultra-high resolution single-photon emission tomography. *Eur J Nucl Med*. 2002;29:691–698.
4. Gourion D, Noll D. The inverse problem of emission tomography. *Inverse Problems*. 2002;18:1435–1460.

5. Zeng GL, Gagnon D. CdZnTE strip detector SPECT imaging with a slit collimator. *Phys Med Biol*. 2004;49:2257–2271.

6. Schramm NU, Ebel G, Engeland U, Schurrat T, Béhé M, Behr TM. High-resolution SPECT using multipinhole collimation. *IEEE Trans Nucl Sci*. 2003; 50:315–320.

7. Beekman FJ, McElroy DP, Berger F, Gambhir SS, Hoffman EJ, Cherry SR. Towards in vivo nuclear microscopy: iodine-125 imaging in mice using micropinholes. *Eur J Nucl Med*. 2002;29:933–938.

8. Meikle SR, Kench P, Weisenberger AG, et al. A prototype coded aperture detector for small animal SPECT. *IEEE Trans Nucl Sci*. 2002;49:2167–2171.

9. Beekman FJ, Vastenhouw B. Design and simulation of a high-resolution stationary SPECT system for small animals. *Phys Med Biol*. 2004;49:4579–4592.

10. Metzler SD, Greer KL, Jaszczak RJ. Helical pinhole SPECT for small-animal imaging: a method for addressing sampling completeness. *IEEE Trans Nucl Sci*. 2003;50:1575–1583.

11. Kudo H, Saito T. Exact cone-beam reconstruction with a new completeness condition. In: Grangeat P, ed. *Proceedings of the International Meeting on Fully Three-Dimensional Image Reconstruction in Radiology and Nuclear Medicine*. Aix-les-Bains, France: CEA; 1995:255–259.

12. Zeng GL, Gullberg GT, Foresti SA. Eigen analysis of cone–beam scanning geometries. In: Grangeat P, ed. *Proceedings of the International Meeting on Fully Three-Dimensional Image Reconstruction in Radiology and Nuclear Medicine*. Aix-les-Bains, France: CEA; 1995:261–265.

13. Walrand S, van Dulmen A, van Rossem H, Pauwels S. Acquisition of linogram in SPECT: implementation and benefits. *Eur J Nucl Med*. 2002;29:1188–1197.

14. Edholm P, Herman GT, Roberts DA. Image reconstruction from linograms: implementation and evaluation. *IEEE Trans Med Imaging*. 1988;7:239–246.

15. van Dulmen A, Walrand S, inventors; van Dulmen A, assignee. Method of imaging by SPECT. European patent EP 1 247 280. October 9, 2002.

16. Brasse D, Piqueras I, Guyonnet JL. Development of a high resolution SPECT system dedicated to small animal imaging. In: Nuclear Science Symposium Conference Record. Piscataway, NJ: IEEE; 2004;3868–3871.

17. Shepp LA, Vardi Y. Maximum likelihood reconstruction for emission tomography. *IEEE Trans Med Imaging*. 1982;2:113–122.

18. Lange K, Carson R. EM reconstruction algorithms for emission and transmission tomography. *J Comput Assist Tomogr*. 1984;8:306–316.

19. Hamill J, Michel C, Kinahan P. Fast PET EM reconstruction from linograms. *IEEE Trans Nucl Sci*. 2003;50:1630–1635.

20. Hubbel JH, Seltzer SM. Tables of X-ray mass attenuation coefficients and mass energy-absorption coefficients from 1 keV to 20 MeV for elements Z = 1 to 92 and 48 additional substances of dosimetric interest, 1989, 1990, 1996. Available at: http://physics.nist.gov/PhysRefData/XrayMassCoef/cover.html. Accessed April 18, 2005.

21. Magnusson M. *Linogram and Other Direct Fourier Methods for Tomographic Reconstruction* [dissertation]. Linköping, Sweden: Linköping Studies in Science and Technology, Dissertation 320, Linköping University; 1993.

22. Averbuch A, Coifman RR, Donoho Dl, Israeli M, Waldén J. Fast slant stack: a notion of radon transform for data in a cartesian grid which is rapidly computable, algebraically exact, geometrically faithful and invertible. Technical reports 2001, Department of Statistics, Stanford University. Available at: http://www-stat.stanford.edu/~donoho/reports/2001/FastSlantStack.ps.Z. Accessed April 18, 2005.

23. Zeng L. Processing of projections with oversampling. UCAIR Symposia, Alta Lodge, UT, October 8, 1999. Available at: http://www.ucair.med.utah.edu/Symposia/symposium-1999.html. Accessed May 04, 2005.